Development/Plasticity/Repair

Mlc1-Expressing Perivascular Astrocytes Promote Blood–Brain Barrier Integrity

John E. Morales, Arpan De, Alexandra A. Miller, Zhihua Chen, and Joseph H. McCarty
Department of Neurosurgery and Brain Tumor Center, University of Texas M. D. Anderson Cancer Center, Houston, Texas 77030

In the mammalian brain, perivascular astrocytes (PAs) closely juxtapose blood vessels and are postulated to have important roles in the control of vascular physiology, including regulation of the blood–brain barrier (BBB). Deciphering specific functions for PAs in BBB biology, however, has been limited by the ability to distinguish these cells from other astrocyte populations. In order to characterize selective roles for PAs *in vivo*, a new mouse model has been generated in which the endogenous megalencephalic leukoencephalopathy with subcortical cysts 1 (Mlc1) gene drives expression of Cre fused to a mutated estrogen ligand-binding domain (Mlc1-T2A-CreERT2). This knock-in mouse model, which we term MLCT, allows for selective identification and tracking of PAs in the postnatal brain. We also demonstrate that MLCT-mediated ablation of PAs causes severe defects in BBB integrity, resulting in premature death. PA loss results in aberrant localization of Claudin 5 and -VE-Cadherin in endothelial cell junctions as well as robust microgliosis. Collectively, these data reveal essential functions for Mlc1-expressing PAs in regulating endothelial barrier integrity in mice and indicate that primary defects in astrocytes that cause BBB breakdown may contribute to human neurologic disorders.

Key words: **angiogenesis; endothelial cell; juxtavascular; megalencephalic leukoencephalopathy with subcortical cysts 1; microenvironment; neurovascular**

Significance Statement

Interlaced among the billions of neurons and glia in the mammalian brain is an elaborate network of blood vessels. Signals from the brain parenchyma control the unique permeability properties of cerebral blood vessels known as the blood–brain barrier (BBB). However, we understand very little about the relative contributions of different neural cell types in the regulation of BBB functions. Here, we show that a specific subpopulation of astrocyte is essential for control of BBB integrity, with ablation of these cells leading to defects in endothelial cell junctions, BBB breakdown, and resulting neurologic deficits.

Introduction

Astrocytes are a heterogeneous collection of glial cells that play essential roles in CNS development and physiology (Khakh and Deneen, 2019). Perivascular astrocytes (PAs), which intimately associate with blood vessels, likely have important physiological roles in neurovascular biology, including control of blood–brain barrier (BBB) permeability (O'Brown et al., 2018). Functions for PAs at the BBB are based in large part on *in vitro* studies; for example, astrocytes cocultured with endothelial cells induce expression of tight junction proteins, promote increased electrical resistance, and suppress the transport of small molecules and ions (Helms et al., 2016). Early *in vivo* studies in rodents supported the premise that astrocytes are essential for endothelial barrier formation (Janzer and Raff, 1987). However, the physiological relevance of experimental systems involving non-CNS endothelial cells and astrocyte aggregates implanted in the rat eye or embedded in the chicken chorioallantoic membrane have been disputed (Holash et al., 1993). Indeed, astrocytes are known to control cerebral blood flow and metabolism (MacVicar and Newman, 2015) and have other critical physiological roles in the brain (Cohen-Salmon et al., 2021), suggesting that their perivascular location could be unrelated to the BBB. In addition, PAs are associated with the glymphatic system, which plays important roles in the clearance of toxic metabolites from the mammalian brain (Rasmussen et al., 2018). Therefore, rather than having direct roles in regulating BBB physiology, PAs may instead be positioned to respond to pathologic alterations in the BBB and/or the glymphatic system (Heinemann et al., 2012).

In vivo studies of PAs have been hindered by the lack of models that distinguish these cells from other astrocyte populations. For example, mouse models using promoters for glial fibrillary acidic protein (Gfap) (Guo et al., 2017), aldehyde dehydrogenase

Received Sep. 13, 2021; revised Nov. 20, 2021; accepted Dec. 8, 2021.

Author contributions: J.E.M., A.A.M., Z.C., and J.H.M. performed research; J.E.M., A.D., A.A.M., and J.H.M. edited the paper; A.D., A.A.M., Z.C., and J.M. analyzed data; J.M. designed research; J.H.M. wrote the first draft of the paper.

This work was supported in part by National Institutes of Health Grants R01NS087635, R21NS103841, and P50CA127001; the Cancer Prevention and Research Institute of Texas RP180220; the Brockman Foundation; and the Terry L. Chandler Foundation (TLC^2).

The authors declare no competing financial interests.

Correspondence should be addressed to Joseph H. McCarty at jhmccarty@mdanderson.org.

https://doi.org/10.1523/JNEUROSCI.1918-21.2021

Copyright © 2022 the authors

1 family member L1 (Aldh1l1) (Winchenbach et al., 2016), or glutamate aspartate transporter (Slc1a3) (Regan et al., 2007) show activities in multiple astrocyte populations. Therefore, ablation of astrocytes using the broadly active GLAST or GFAP promoters does not discern the PA population from non-PA populations (Heithoff et al., 2021; Williamson et al., 2021). Thus, more selective models for identification of PAs are necessary for determining the exact functions of these cells *in vivo*.

In order to selectively target PAs *in vivo*, we have focused on the megalencephalic leukoencephalopathy with subcortical cysts 1 gene (Mlc1) gene. In the mammalian brain, Mlc1 shows exclusive expression in PAs (van der Knaap et al., 2012; Estévez et al., 2018; Lattier et al., 2020). Mlc1 encodes an integral membrane protein that has sequence homology to voltage-gated potassium channels (Boor et al., 2005). Published reports have identified Mlc1-interacting adhesion proteins such as GlialCAM (Alonso-Gardon et al., 2021), chloride channels such as CLCN2 (Gaitán-Peñas et al., 2017), and gap junction proteins such as connexin 43 (Lanciotti et al., 2020). Mlc1 also suppresses the enzymatic activities of receptor tyrosine kinases such as EGFR (Brignone et al., 2019) and Axl (Lattier et al., 2020). In patients with MLC1 mutations and in $Mlc1^{-/-}$ mice, neurologic deficits are associated with astrocyte swelling and white matter cavitations (Dubey et al., 2018).

Here we have generated a knock-in mouse model in which the endogenous Mlc1 gene drives expression of CreERT2 (Mlc1-T2A-CreERT2 or MLCT). MLCT activities are induced by tamoxifen in PAs but not in other neurovascular cell components, including neurons, endothelial cells, or nonastrocytic glial cells. Selective ablation of PAs *in vivo* using MLCT results in severe BBB pathologies and premature death. Disruption in endothelial cell permeability is linked to altered expression patterns of key BBB proteins such as Cld5 and VE-Cadherin. PA ablation also leads to neuroinflammatory responses as evidenced by microglial activation. Collectively, these results provide direct *in vivo* evidence that PAs, and specifically those that express Mlc1, provide essential functions in regulation of BBB physiology in the adult brain.

Materials and Methods

Generation of the MLCT mouse model. This study was reviewed and approved by the M. D. Anderson Cancer Center Institutional Animal Care and Use Committee in compliance with the National Research Council's *Guide for the care and use of laboratory animals*. The approved protocol number is ACUF-00001108-RN02. To generate the MLCT knock-in model, a 9.4 kb region used to construct the targeting vector was first subcloned from BAC clone RP23-268N19 using homologous recombination-based technique. The vector was designed such that the long homology arm extends ~5.9 kb upstream of the T2A-CreERT2 cassette and the short homology arm extends 2.2 kb downstream of the Neo cassette. The T2A-CreERT2 cassette was inserted immediately upstream of the endogenous stop codon of the Mlc1 gene. The FRT flanked Neo selection cassette was inserted 116 bp downstream of the 3′ UTR. The total size of the targeting construct (including vector backbone and diphtheria toxin [DT] cassette) is ~18.2 kb. The region was designed such that the long homology arm extends 6.4 kb to the exon 12 of Mlc1 gene, and the CreERT2 reporter is fused in frame to exon 12 so that CreERT2 uses the endogenous polyadenylation tail of Mlc1 to terminate the transcript.

The targeting vector was linearized with NotI and then transfected by electroporation of FLP 129/SvEv x C57Bl/6 (HF4) embryonic stem (ES) cells. After selection with G418 antibiotic, surviving clones were expanded for PCR analysis to identify recombinant ES clones. The Neo cassette in the targeting vector was removed during ES clone expansion. Flp-expressing ES cells were verified for deletion of the neomycin cassette. Two different clones were microinjected into C57bl/6 mice, generating chimeras with high-percentage agouti coat color. Subsequent breeding with WT C57bl/6 mice produced heterozygous MLCT mice. Genotyping identification of MLCT mice was performed using genomic PCR screening with DNA isolated from tail snips taken from pups with agouti or black coat color. The boundaries of the vector and genomic sequences were confirmed by sequencing primers P6 and T73. Primer N2 and N3 read from the Neo selection cassette into the 3′ end of the 3′ UTR and the 5′ end of the short homology arm, respectively. Litters were average size, between 5 and 8 pups. Adult heterozygous and homozygous mice are fertile and have survived for more 10 months without obvious phenotypes. Oligonucleotides used to confirm gene targeting are as follows: P6: 5′-GAG TGC ACC ATA TGG ACA TAT TGT C-3′; T73: 5′-TAA TGC AGG TTA ACC TGG CTT ATC G-3′; iNeo N2: 5′-AGT ATG GCT TTC CTT CCC GAT GG-3′; IVNeo N3: 5′- TCT AAG GCC GAG TCT TAT GAG CAG-3′; SQ1: 5′-CCA CAC AGA CTC AGC CGA ATC TG-3′; SQ2: 5′-ACA TTG GCA GGA CCA AGA CCC TG-3′; SQ3: 5′- GCT GGT TCA CAT GAT CAA CTG GGC-3′; P1: 5′-TGG ACC TAT GGA TAT CTC CAA CCT GCT GAC TGT GCA C-3′; PNDEL1: 5′- TGC TTC TGG GGA AAA AGG GTT-3′; and PNDEL2: 5′- GGT GCC TTG GGT TGT CTT GA-3′.

Sequencing was performed using purified genomic DNA to confirm the 5′ junction of the CreERT2 cassette using the SQ1 primer. A PCR was performed on clones to confirm retention of the CreERT2 cassette knocked-in using the SQ1 and FN2A primers. This reaction produces a product of 3.52 kb in size in the presence of CreERT2 cassette. Genomic DNA analysis using primers PNDEL1 and PNDEL2 was performed with mouse tail snips to screen for the deletion of the Neo cassette, yielding a 430 bp product for the WT allele and a 514 bp product for the knock-in allele.

Tamoxifen and DT injections. To activate CreERT2, MLCT pups were injected intragastrically for 3 consecutive days (P1-P3) with 50 µl of 1 mg/ml tamoxifen (Sigma-Aldrich, T5648) using a 10 mg/ml stock solution prepared as follows: 10 mg of tamoxifen was dissolved in 250 µl of 100% ethanol, and 750 µl of sterile sunflower seed oil (Sigma-Aldrich, S5007) and vortexed until emulsified. This stock solution was stored in the dark at 4°C for up to 3 d. On each day of use, a working solution was prepared fresh by a 1:10 dilution of the stock solution in sunflower seed oil. To ablate cells expressing DT receptor (DTR) following Cre-induced expression, mouse pups were injected intraperitoneally for 5 d at ages P7 to P12 with 50 µl of a 2 µg/ml working solution of DT. A 2 mg/ml stock DT solution was prepared by dissolving 1 mg of DT powder (Sigma, D0564) in 0.5 ml of sterile water. On each day of use, a 2 µg/ml working solution was prepared fresh by diluting 5 µl of stock DTA solution in 5 ml of sterile 10 mM Tris, pH 7.4, 1 mM EDTA.

Immunofluorescence experiments. Mice were anesthetized at different time points, and bodies were fixed by cardiac perfusion of 4% PFA in PBS. Brains were removed and immersed in 4% PFA for an additional 24 h at 4°C. After fixation, brains were embedded in 4% agarose and sectioned at 100 µm on a vibratome and stored in PBS at 4°C. Alternatively, brains were processed for paraffin embedding and sectioning. Sections were permeabilized and blocked with 10% donkey serum in PBS-T (1XPBS supplemented with 0.1% Triton X-100) for 1 h at room temperature, followed by an overnight 4°C incubation with primary unconjugated antibodies diluted in the blocking solution. Immunofluorescence analyses were performed with the following primary antibodies: Albumin (Mybiosource, MBS2001910), Calbindin (Swant, D-28k), CD31 (BD Biosciences, 553370), CD31 (R&D Systems, AF3628), Claudin 5 (Thermo Fisher Scientific, 35-2500), GFP (Abcam, ab290), GFP (Abcam, ab13970), GFAP (DAKO, Z0334), GFAP (Novus, NBP1-05198), Iba1 (WAKO, 01919741), Laminin (Sigma, L9393), MBP (Abcam, ab40390), NG2 (AB5320), Sox9 (Ab185966), and VE-Cadherin (BD PharMingen, 550548). The sections were then washed with PBS-T and incubated with secondary antibodies (1:500 dilution) in the blocking solution for 2 h. Sections were again washed 3 times with 1× PBS-T, then briefly washed with 1× PBS. The sections were mounted on pretreated microscope slides, sealed using Vectashield with DAPI mounting media (Vector Laboratories), and kept at 4°C until imaging. Confocal images were acquired using an Olympus Fluoview FV3000

10×, 20×, and 30× objectives. All comparative images were taken with the same laser power and gain settings to make qualitative comparisons between staining levels in different samples. Multiple FOVs were imaged from biological replicates.

Retinal whole-mount immunostaining. Enucleated eyes from P7 and P14 mice were fixed in ice-cold 4% PFA in PBS for 1 h and washed 3 times in ice-cold PBS. Retinas were carefully isolated under a Leica S6E dissecting stereomicroscope (Leica Microsystems) and mounted onto microscope slides. Whole retinas were permeabilized and blocked in 10% normal donkey serum diluted in PBS-T for 1 h at room temperature. Primary antibodies against GFAP, GFP, and CD31 were diluted in the blocking buffer and incubated overnight at 4°C. Retinas were then washed 3 times in PBST for 30 min. Secondary antibodies against primary host species were diluted in blocking buffer (1:500 dilution) and added to retinas to incubate at room temperature for 2 h. Retinas were again washed 3 times in PBST for 30 min and sealed under coverslips using Vectashield mounting medium and stored at 4°C until imaging.

Image acquisition and analysis. Immunofluorescence images were acquired using an Olympus Fluoview FV3000 confocal laser scanning microscope. Multidimensional acquisition was conducted using *Z* stacks with <2.5 mm slicing intervals at a scan rate of 4 μs/pixel with a resolution of at least 1024 × 1024 pixels per slice and digitally compiled in FV31S-SW (version 2.4.1.198). Image acquisition parameters, including exposure time, laser power, gain, and voltages, were fixed for each imaging channel. Immunohistochemistry-labeled images were captured using an Olympus BX43 light microscope.

All images were analyzed using ImageJ and Fiji (National Institutes of Health) (Schindelin et al., 2012; Schneider et al., 2012). Serial *Z*-stack images (3 slices per image) were used for Iba1 quantitation to determine Iba1$^+$ microglial cell parameters, and all images were scaled (μm) as per the objective lens used for acquisition. Image stacks were projected for maximum intensity to include all Iba1 signals, but auto-threshold module was then used to include only cellular signals for quantitation. Cellular parameters (cell count, area coverage, mean fluorescence intensity, major and minor axes as shape descriptors, and circularity) were quantitated using "analyze particles" algorithm. This module counted Iba1$^+$ microglial cells above the set threshold of 50 μm^2 to avoid any nonspecific background and/or noise. Integrated density measures total cellular fluorescence intensity based on the area coverage per cell. Thus, a cell with higher area coverage and/or mean signal intensity gives higher integrated density values. The major and minor axes measure the maximum and minimum distances between two points on the cell periphery. A completely circular shape will have identical major and minor axes values, whereas the difference between the major and minor axes will increase as the cell becomes less circular and attains more ameboid or elongated morphology. Shape factor determines such differences between major and minor cellular axes to validate cell morphology. Fluorescence signal intensity of channels were measured using the standard "color histogram" module in ImageJ.

Isolation and analysis of primary brain astrocytes. Primary mouse astrocytes were cultured as described previously (McCarty et al., 2005). Briefly, mouse pups at postnatal day 3 (P3) were genotyped, killed, and whole brains were removed and subjected to enzymatic dissociation in a papain-containing buffer (Miltenyi Biotec, #130-095-942). Dissociated cells at high density were resuspended in low-glucose DMEM (Hyclone) containing 10% FBS with 1% penicillin/streptomycin and seeded to laminin (Sigma)-coated dishes. Adherent astrocytes were cultured to confluence for 7 d and passaged no more than 3 times before any experimentation as previously described (Hirota et al., 2015; Lee et al., 2015). Whole-cell lysates were collected under normal culture conditions in 1% NP-40 (50 mM Tris-HCl, pH 8.0, 150 mM NaCl) lysis buffer with protease and phosphatase inhibitor tablets (Roche). Total protein was measured by BCA assay (Pierce) and then denatured at 95C for 5 min in 5× SDS loading buffer containing 2.5% 2-mercaptoethanol (Sigma), and 15 mg of protein was resolved on 10% Tris-glycine gels. Immunoblotting was performed with nitrocellulose membranes (Bio-Rad), blocked using Odyssey TBS-based blocking buffer (LI-COR), and then incubated with specific primary antibodies diluted in blocking buffer supplemented with 0.1% Tween-20 overnight at 4C. Target proteins were normalized to total cellular/housekeeping protein, α-actinin (LI-COR). Secondary antibodies (IRDye 800CW goat anti-rabbit and IRDye 680RD goat anti-mouse; LI-COR) were incubated in the dark at room temperature for 40 min. Dual-channel infrared scan and quantitation of immunoblots were conducted using the Odyssey CLx infrared imaging system with Image Studio (version 5.2, LI-COR).

Statistical analyses. All quantitation of confocal images were performed using Image J (National Institutes of Health) (Schindelin et al., 2012; Rueden et al., 2017). GraphPad prism 9.0 was used to plot mean values ($n = 3$ or greater ± SEM, unless otherwise indicated) to compare between experimental and control groups and to determine statistical differences by unpaired Student's t test and two-way ANOVA (Tukey *post hoc* analysis) at 95% CIs (α value 0.05).

Results

Development of the MLCT mouse model

We engineered a T2A knock-in mouse model in which the endogenous Mlc1 gene drives expression of CreERT2, which can be selectively activated by exposure to tamoxifen (Cleaver, 2021). The T2A-CreERT2 cDNA was inserted in the open reading frame of Mlc1 in exon 12 to allow the ribosome to translate through the T2A-CreERT2 sequence. Termination is initiated at the 3' UTR (exon 12) where the endogenous poly A sequence is located, resulting in independent expression of the endogenous Mlc1 gene product and the T2A-CreERT2 product (Fig. 1*A*). After Flp-mediated deletion of the neomycin cassette, a single FRT site remains in MLCT/+ heterozygous mice (Fig. 1*A*). The genotypes of WT and heterozygous (MLCT/+) mice can be differentiated by genomic PCR (Fig. 1*B*). MLCT/+ heterozygous and MLCT/MLCT homozygous knock-in mice were viable and fertile. Astrocytes were cultured from the cerebral cortices of P5 WT control or MLCT/+ pups. As shown in Figure 1*C*, *D*, immunoblot analysis of detergent-soluble cell lysates revealed that the Mlc1 protein was expressed in MLCT/+ cells at similar levels as WT control cells. These data for Mlc1 protein expression in astrocytes match Mlc1 mRNA expression patterns in mouse brain single-cell transcriptome datasets (Vanlandewijck et al., 2018).

Tamoxifen induction of MLCT activities in PAs *in vivo*

In order to analyze spatial patterns of MLCT activities, we interbred MLCT/+ male mice with Rosa26-loxSTOPlox-YFP/+ (R26-YFP) female mice. The R26-YFP reporter strain allows for Cre-mediated activation of YFP expression following tamoxifen-induced recombination of the floxed STOP cassette (Srinivas et al., 2001). The experimental strategy for testing MLCT activities using the R26-YFP reporter strain is summarized in Figure 1*E*. Expression of YFP was not detected in brain tissue from R26-YFP mice (MLCT-negative and not injected with tamoxifen) (Fig. 2*A*,*B*). Next, P7, P14, and P30 mice were killed, and YFP expression patterns were analyzed in fixed tissues. Double immunofluorescence labeling was used to analyze the cerebral cortex, hippocampus, and thalamus using an anti-GFP antibody (which cross-reacts with YFP) in combination with antibodies against GFAP (astrocytes) or CD31 (vascular endothelial cells). Robust YFP expression was detected in many GFAP-expressing cells (Fig. 2*C–E*) adjacent to CD31$^+$ blood vessels in the various brain regions analyzed (Fig. 2*F–H*). Vascular endothelial cells were negative for YFP expression, with confocal analysis of serial sections showing a clear demarcation between YFP$^+$ astrocytes and CD31$^+$ endothelial cells (Fig. 2*F–H*). At P7, which is a robust time of astrocyte differentiation in the mouse brain (Zarei-Kheirabadi et al., 2020), YFP$^+$ PAs showed multipolar morphologies and were

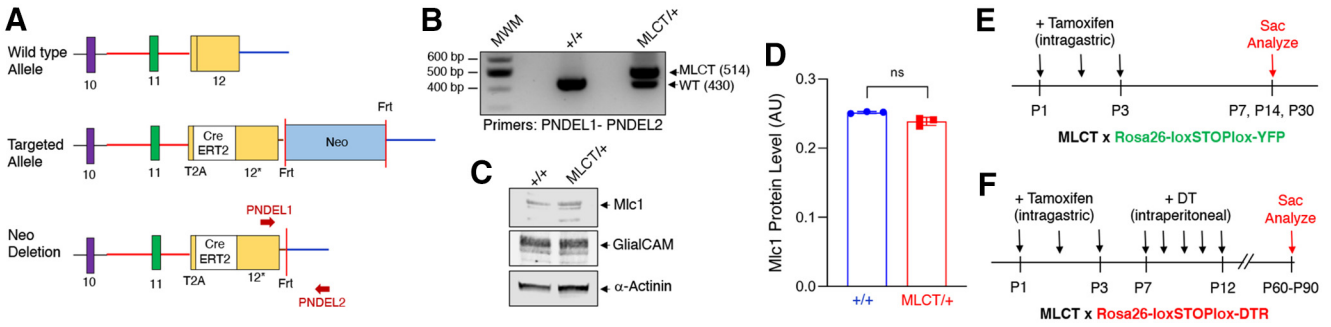

Figure 1. Generation and characterization of the MLCT knock-in mouse model. ***A***, Strategy to express CreERT2 via the endogenous Mlc1 promoter based on T2A peptide skipping. The schematic shows the 3′ region of the murine Mlc1 locus (top) containing exons 9-12, and the targeted Mlc1 locus before (middle) and after (bottom) Flp-mediated excision of the Neomycin cassette. Red arrows indicate primers used for PCR-based validation of cassette insertion. ***B***, PCR genotyping using genomic DNA isolated from tail snips distinguishes WT (+/+) and heterozygous (MLCT/+) mice. ***C***, Detergent-soluble lysates from WT control or MLCT/+ mouse astrocytes isolated from P5 pups were immunolabeled with anti-GLIALCAM or anti-Mlc1, revealing normal levels of protein expression. The α-actinin immunoblot serves as a loading control. ***D***, Quantitation of Mlc1 protein levels in WT and MLCT/+ brain lysates based on the immunoblotting data in ***C***. Densitometry was performed to determine Mlc1 levels in relation to the α-actinin loading control. ***E***, ***F***, Experimental strategies to analyze MLCT activities in R26-YFP mice following tamoxifen injection (***E***) or in R26-DTR mice injected sequentially with tamoxifen and DT (***F***).

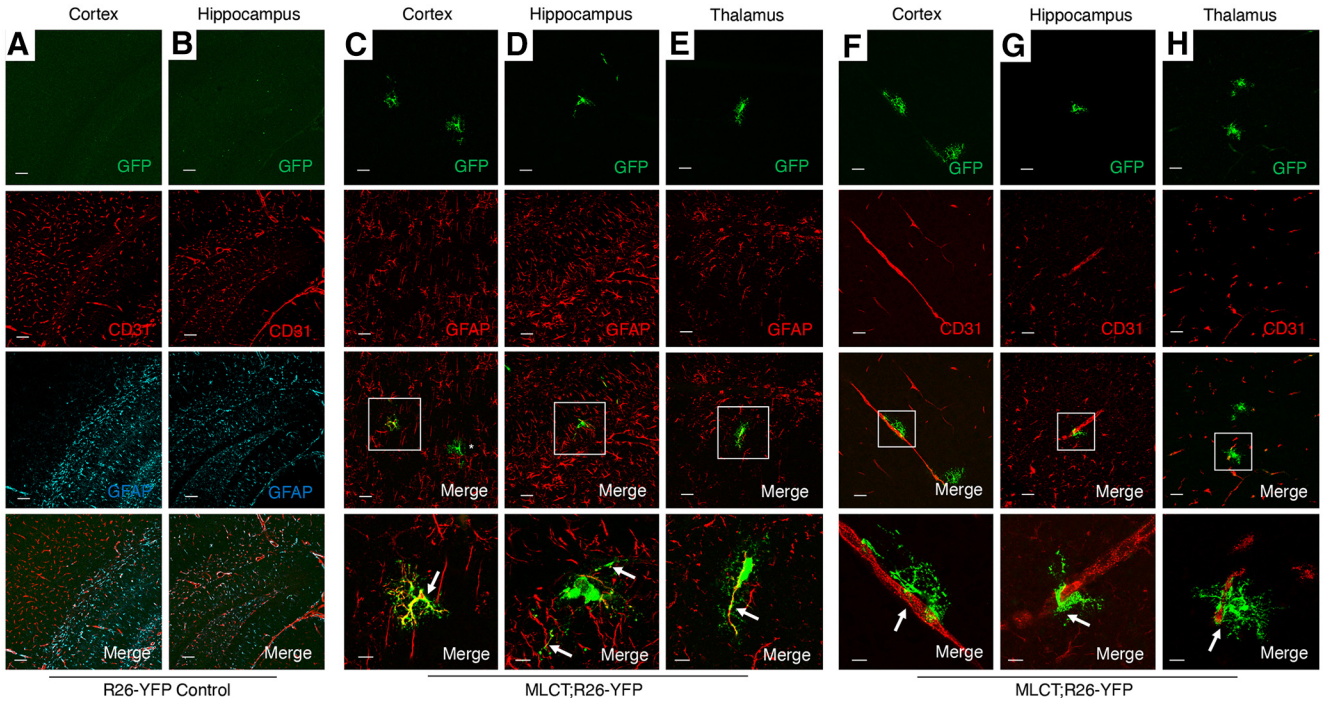

Figure 2. MLCT is active in subpopulations of astrocytes in the P7 brain. ***A***, ***B***, R26-YFP control mouse pups (MLCT-negative) were injected with tamoxifen from P1-P3, and brains were harvested at P7. Coronal sections were analyzed by triple immunofluorescence using anti-GFP (green), anti-CD31 (red), and anti-GFAP (cyan) antibodies. Note the lack of expression of YFP in the cortex (***A***) and hippocampus (***B***). ***C–E***, MLCT;R26-YFP mouse pups were injected with tamoxifen from P1-P3, and brains were harvested at P7. Coronal brain sections were analyzed by double immunofluorescence using anti-GFP (green) and anti-GFAP (red) antibodies. Note the coexpression of YFP and GFAP in some astrocytes of the cortex (***C***), hippocampus (***D***), and thalamus (***E***). There are also YFP-expressing cells that lack GFAP expression (see asterisk in lower magnification panel in ***C***). Bottom panels ***C–E*** are higher-magnification images of boxed areas in the lower-magnification merged panels. ***F–H***, MLCT;R26-YFP mouse pups were injected with tamoxifen from P1-P3, and brains were harvested at P7. Coronal brain sections were analyzed by double immunofluorescence using anti-GFP (green) and anti-CD31 (red) antibodies. Note the YFP$^+$ cells adjacent in blood vessels in the cortex (***F***), hippocampus (***G***), and thalamus (***H***). Bottom panels ***F–H*** are higher-magnification images of boxed areas in the lower magnification merged panels. Scale bar, 100 μm.

juxtaposed with individual blood vessels. These data for Mlc1 gene expression in MLCT;R26-YFP mice match our prior results showing Mlc1 protein in PAs of Mlc1-T2A-GFP mice (Toutounchian and McCarty, 2017) as well as astrocyte expression of Mlc1 in transcriptome analyses of brain neural and vascular cells (Zhang et al., 2014).

Analysis of brains from MLCT;R26-YFP mice at P14, a time when astrogenesis has mostly concluded, revealed continued coexpression of YFP and GFAP in astrocytes adjacent to CD31-expressing blood vessels in various regions of the brain, including in the cortex, corpus callosum, thalamus, and cerebellar white matter (Fig. 3*A–D*). MLCT was also active in GFAP-expressing Bergmann glia, which have cell bodies located within the Purkinje layer and project multiple processes that span the molecular layer and terminate at the P14 pial surface (Fig. 3*E*). Indeed, the somas of YFP-expressing cells are located between larger Purkinje neurons, as revealed by immunolabeling P30 sections with anti-laminin antibodies (Fig. 3*E*). YFP-expressing PAs

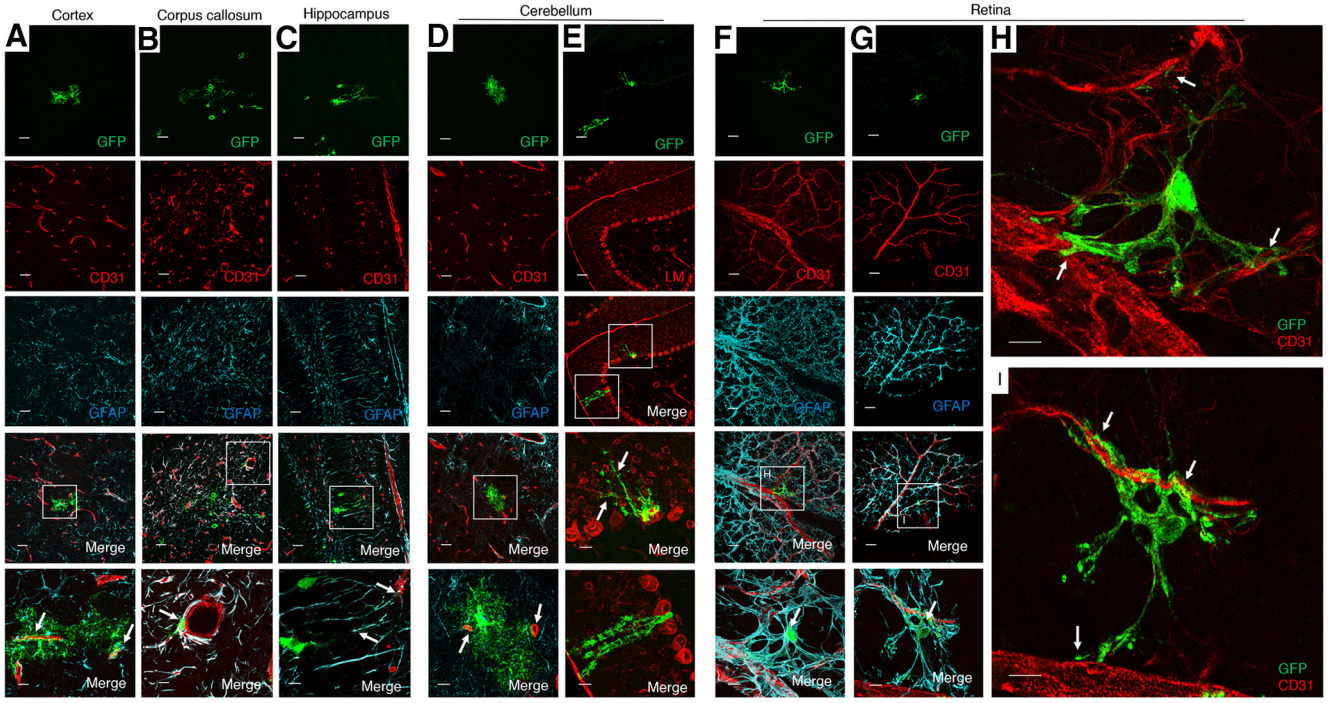

Figure 3. Selective activation of MLCT in PAs of the P14 brain. ***A–D***, MLCT;R26-YFP mouse pups were injected with tamoxifen from P1-P3, and brains were harvested at P14. Coronal sections were analyzed by triple immunofluorescence using anti-GFP (green), anti-CD31 (red), and anti-GFAP (cyan) antibodies. Note the coexpression of YFP and GFAP in some astrocytes of the cortex (***A***), corpus callosum (***B***), hippocampal dentate gyrus (***C***), and cerebellum (***D***). While many YFP$^+$ PAs are also GFAP$^+$, we detect some PAs that lack GFAP expression; for example, note the YFP$^+$ PA in the cerebellar white matter that lack obvious GFAP expression (arrows in ***D***). ***A–D***, Bottom, Higher-magnification images of boxed areas in the lower-magnification merged panels. ***E***, Representative image of a sagittal section through the MLCT;R26-YFP cerebellum at P30 analyzed by double immunofluorescence using anti-GFP (green) and anti-Laminin (red) antibodies. YFP$^+$ Bergmann astrocytes are also GFAP$^+$ (arrows), and Bergmann astrocyte cell bodies are located between Laminin$^+$ Purkinje neuron cell bodies and extend elaborate processes (arrows). ***F***, ***G***, Flat-mounted retinas P14 MLCT;R26-YFP mice were analyzed by triple immunofluorescence using an anti-GFP antibody (green) in combination with anti-CD31 (red) and anti-GFAP antibodies (cyan). Note the overlapping YFP/GFAP expression in astrocytes of the P14 retinal primary vascular plexus (arrows in merged images, ***F*** and ***G***). ***H***, ***I***, Higher-magnification images of boxed areas in ***F*** and ***G***, respectively, showing only anti-GFP (green) and anti-CD31 (red) merged channels. Note the close juxtaposition between YFP$^+$ PAs and CD31$^+$ blood vessels (arrows). Scale bars, 100 μm.

at P14 showed a more elaborate cytoarchitecture with multiple projections that often contacted more than one blood vessel (Fig. 3). We also detected more heterogeneity in the morphologies of PAs at P14, with cells in the cortex and cerebellar white matter showing multipolar cytoarchitectures, whereas cells in the corpus callosum and hippocampus displayed radial glial-like appearances (Fig. 3). In the P14 retina, YFP expression showed overlap with GFAP$^+$ cells, and there was also close juxtaposition between YFP$^+$ cells and CD31-expressing endothelial cells (Fig. 3*F–I*). Individual retinal PAs extended multiple processes that contacted several blood vessels (Fig. 3*H*,*I*). These data suggest that Mlc1-expressing PAs may promote the formation and/or stability of the blood-retinal barrier. Iba1$^+$ microglia were detected in close juxtaposition with YFP-expressing PAs in the P14 brain; however, YFP and Iba1 coexpression was not detected in microglia (Fig. 4).

Ablation of PAs leads to pathologic BBB integrity

We next used a mouse model in which the cDNA encoding the DTR is inserted in the Rosa26 locus (R26-loxSTOPlox-DTR) allowing for Cre-mediated expression of DTR (Buch et al., 2005). Murine cells are largely resistant to the apoptotic effects of DT because of the absence of DTR (also known as heparin-binding epidermal growth factor-like growth factor precursor 12 protein); however, expression of DTR makes cells susceptible to DT-mediated cell death. Using the R26-loxSTOPlox-DTR model, effects of MLCT-dependent PA ablation on BBB physiology were investigated. The experimental schema for ablating PAs and analyzing effects in MLCT;R26-DTR mice is summarized in Figure 1*F*. Mice receiving sequential tamoxifen and DT injections were viable and did not display obvious phenotypes immediately after treatment. However, at 2-4 months after the last DT injection, MLCT;R26-DTR mice displayed decreased body weight, lower limb paresis, and ataxia. Immunofluorescence labeling was performed on coronally sectioned brains from R26-loxSTOPlox-DTR control ($n = 3$) and MLCT;R26-DTR ($n = 3$) mice. We analyzed distribution of the endogenous biomarker mouse serum albumin, which does not normally exit the circulation (Heinemann et al., 2012). In control mice treated with the same regimen of tamoxifen and DT, serum albumin was retained in the lumens of brain blood vessels (Fig. 6*A–C*). In contrast, serum albumin showed clear extravasation across the BBB in MLCT;R26-DTR mice, with robust levels of extravascular albumin protein detected in the cerebral cortex (Fig. 5*D*), hippocampus (Fig. 5*E*), and brainstem (Fig. 5*F*). The serum albumin extravasation was most pronounced in the mutant cerebral cortex and hippocampus, although statistically significant differences were also detected in the brainstem (Fig. 5*G–I*). Analysis of CD31$^+$ blood vessels in the cortex and hippocampus of DT-treated MLCT;R26-DTR mice, which are brain regions where serum albumin extravasation was most evident, revealed reduced astrocyte coverage; indeed, many blood vessels in the PA-ablated hippocampus were devoid of GFAP$^+$ astrocyte end feet (Fig. 5*J*,*K*). Obvious microgliosis as measured by Iba1$^+$

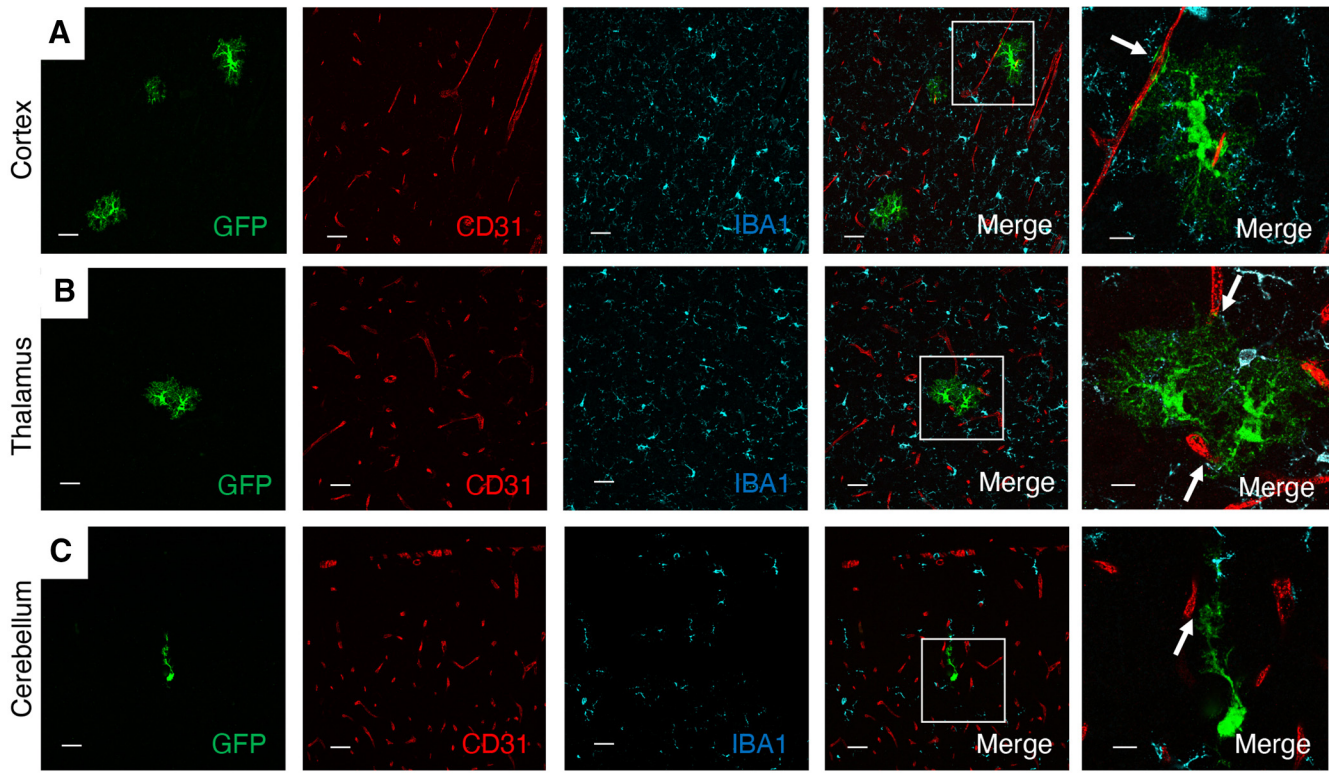

Figure 4. MLCT activities are not detected in Iba1-expressing brain microglial cells. ***A–C***, Representative images of P14 coronal brain sections of MLCT;R26-YFP mice. Brains were sliced coronally, and vibratome sections were analyzed by triple immunofluorescence using anti-GFP (green), anti-CD31 (red), and anti-Iba1 (cyan) antibodies. Merged panels on the far right are higher-magnification images of boxed areas in the lower-magnification merged panels. PAs intimately associate with blood vessels (arrows), but there is no detectable coexpression of YFP and Iba1 in brain microglia in the cortex (***A***), thalamus (***B***), and cerebellum (***C***). Also note the close juxtaposition of YFP^+ PAs and $Iba1^+$ microglia.

immunofluorescence was detected in different brain regions of DT-treated MLCT;R26-DTR mice (Fig. 5*A–D*), although these defects were most pronounced in the mutant cerebral cortex. Various measures of microglial number and activation status based on morphology confirmed neuro-inflammation after PA ablation (Fig. 6*E–G*).

We next analyzed the impact of PA ablation on expression of endothelial cell biomarkers in DT-treated R26-DTR control and MLCT;R26-DTR brain sections. As shown in Figure 7*A*, *B*, we detected altered expression of the tight junction protein Claudin 5 in endothelial cells of DT-treated MLCT;R26-DTR mice. Unlike control mice that display focal patterns of Claudin 5 in tight junctions of endothelial cells, Claudin 5 protein was detected in a more diffuse pattern in cerebral blood vessels of MLCT;R26-DTR mice. Adherens junctions have been reported to promote normal endothelial cell barrier functions via cross-talk with components of tight junctions, including Claudin 5 (Rahimi, 2017). Therefore, we analyzed expression of the adherens junction protein VE-Cadherin. As shown in Figure 7*C*, *D*, a more diffuse expression pattern of VE-Cadherin was detected in vascular endothelial cells following PA ablation. Quantitation of immunofluorescence intensity revealed abnormal patterns of Claudin 5 and VE-Cadherin expression following PA ablation (Fig. 7*E*,*F*). Collectively, these *in vivo* results prove that PAs play crucial roles in maintaining BBB integrity in the mouse brain with loss of these cells leading to BBB disruption and resulting vascular-related neurologic deficits (Fig. 8). Our data suggest that primary genetic or biochemical alterations in PAs that impair normal interactions with blood vessels may contribute to vascular-related developmental and/or adult-onset CNS diseases.

Discussion

Here we report that Mlc1-expressing PAs have essential functions in stabilizing the BBB. To our knowledge, MLCT is the first inducible Cre model that can be activated selectively in PAs but not in other astrocyte populations in the CNS. PAs in MLCT mice were detected around capillaries as well as larger blood vessels in the cerebral cortex, hippocampus, and other regions of the postnatal brain. These results are consistent with a recent immunohistochemical report showing that anti-Mlc1 antibodies label PA processes (Wang et al., 2021), and a quantitative mass spectrometry study showing that Mlc1 protein is highly enriched in PA end feet (Zajec et al., 2021). Although induction of MLCT activities (in the MLCT;R26-YFP model) were specific to PAs in the brain, the numbers of $Mlc1^+$ cells detected were relatively low, with between 3% and 5% of cells showing YFP expression. The low levels of MLCT activities may be because of (1) suboptimal tamoxifen delivery via the intragastric injection route, (2) poor penetration of tamoxifen across the BBB, and/or (3) heterogeneously low levels of CreERT2 protein that can be activated by tamoxifen.

One unresolved question in the glial cell biology field is whether there are distinct subpopulations of astrocytes with neurovascular-specific functions (PAs) or whether all astrocytes interact with blood vessels in some general capacity to influence neurovascular development and homeostasis. Along these lines, a prior publication has shown that nearly 100% of astrocytes in the mouse hippocampus extend end feet that interact with blood vessels as well as neurons and other glial cell types (Foo et al., 2011). We propose that $Mlc1^+$ astrocytes have critical functions in BBB homeostasis, which is supported by the neurovascular

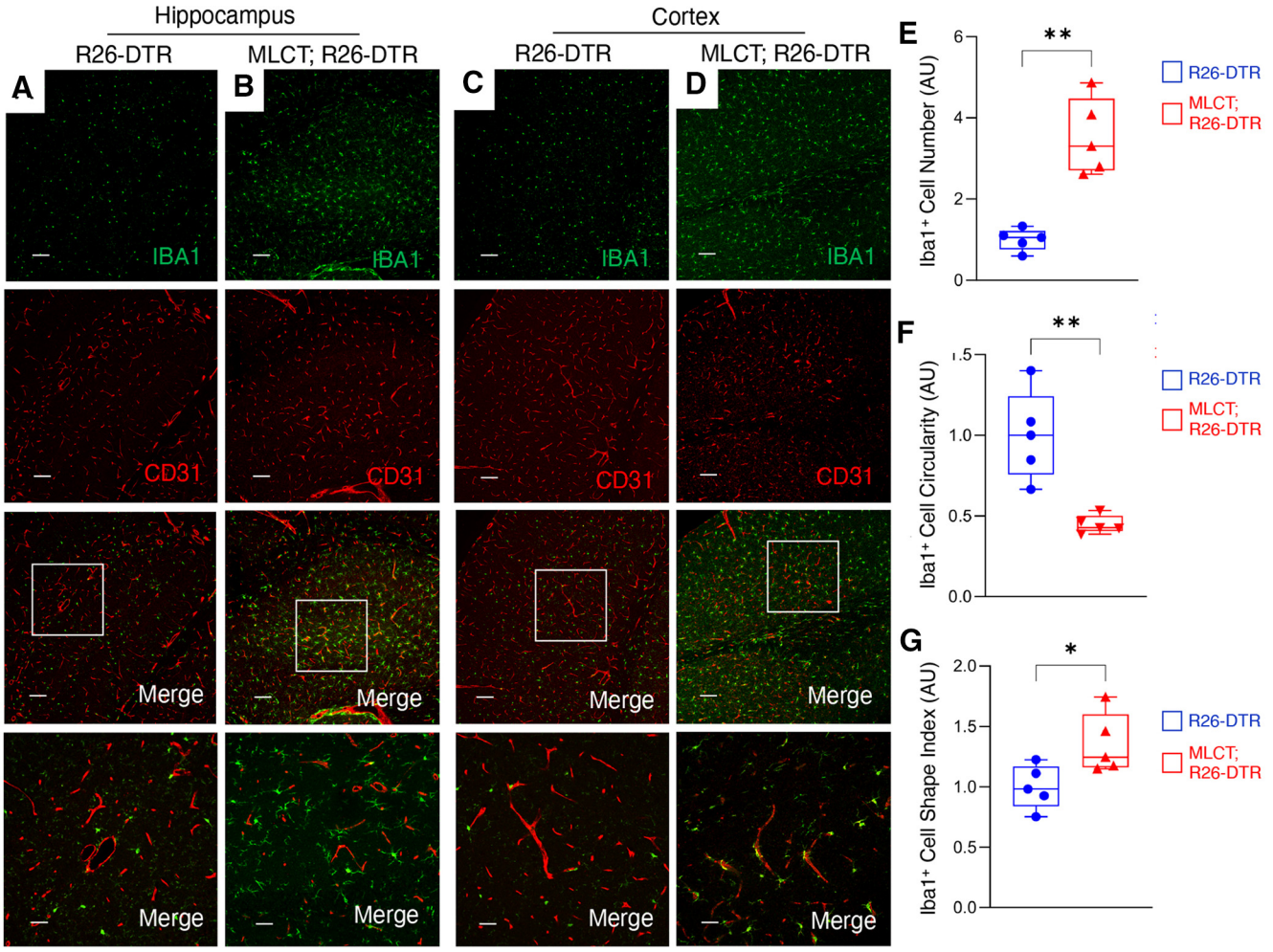

Figure 5. Microgliosis in response to BBB disruption. ***A–D***, Immunofluorescence analysis of P60 coronal sections from one R26-DTR control (***A***) and a MLCT;R26-DTR mutant brain (***B***) labeled with antibodies directed against Iba1 (green) and CD31 (red). Shown are representative images from the hippocampus (***A***,***B***) and cerebral cortex (***C***,***D***). In brain regions from the control mouse (***A***,***C***), there is regular distribution of Iba1-expressing microglia, whereas there is robust perivascular microgliosis in the mutant brains (***B***,***D***), and particularly in cortical regions. ***E–G***, Quantitation of microglial activation in the R26-DTR control cortex and MLCT;R26-DTR mutant cortex as measured by $Iba1^+$ cell number (***E***), circularity (***F***), and shape index (***G***). Differences between groups (***E–G***) were analyzed using Student's *t* test ($n = 3$). Data are mean ± SEM. $^*p < 0.05$. $^{**}p < 0.01$.

pathologies found in $Mlc1^{-/-}$ mice (Gilbert et al., 2021) and in humans with MLC1 mutations (Dubey et al., 2018). Nonetheless, it will be important to determine whether there are other brain pathologies resulting from $Mlc1^+$ astrocyte ablation that are independent of BBB disruption. It is certainly possible that $Mlc1^+$ astrocytes have roles that are independent of their perivascular localization. For example, Mlc1-expressing astrocytes may regulate the functions of other cell types, including neurons and microglia. We detect $Mlc1^+$ astrocytes that are ensheathed by microglia in various regions of the brain. Interestingly, we do not detect significant astrogliosis following PA ablation, suggesting that $Mlc1^+$ cells normally contribute to reactive gliosis, and DT-mediated ablation of these cells blunts the gliosis response. Indeed, in a prior report, we have shown that astrogliosis after traumatic injury to the cerebral cortex involves Mlc1-expressing astrocytes (Toutounchian and McCarty, 2017). The microgliosis we detect in PA-ablated mice is likely a secondary result of BBB pathologies; however, it is also possible that PAs inhibit microglial cell activation, and loss of PAs following DT treatment facilitates microglial activation. It will be important to determine the specific pathways involved in BBB breakdown and microgliosis following PA ablation. In humans, age-dependent BBB dysfunction leads to pathologic serum albumin extravasation, which impacts TGFβ receptor signaling pathways in astrocytes, resulting in microglial activation (Senatorov et al., 2019). Interestingly, a major activator of TGFβ signaling in the brain is $\alpha v\beta 8$ integrin (McCarty, 2020), which is enriched in PAs (Yosef et al., 2020) and may be involved in aberrant TGFβ signaling activation following BBB breakdown.

We propose that the BBB pathologies that develop following PA ablation are linked to loss of proper cell adhesion and communication between PAs and the adjacent vascular endothelium and/or pericytes. Loss of PAs results in defective contact between the astrocyte end feet and the ECM-rich vascular basement membrane, leading to diminished blood vessel structural support and impaired endothelial tight junction integrity. Loss of expression of $Mlc1^+$ PA-derived cues, such as growth factors and cytokines that promote normal endothelial tight junctions and/or vascular basement membrane composition, likely also contribute to BBB pathologies. Astrocytes have been estimated to cover >80% of the abluminal surface of brain capillaries in histologic samples (Saunders et al., 2018), although the extent to which PAs ensheath blood vessels has been questioned recently based on analysis of unfixed tissue samples (Korogod et al., 2015). Our

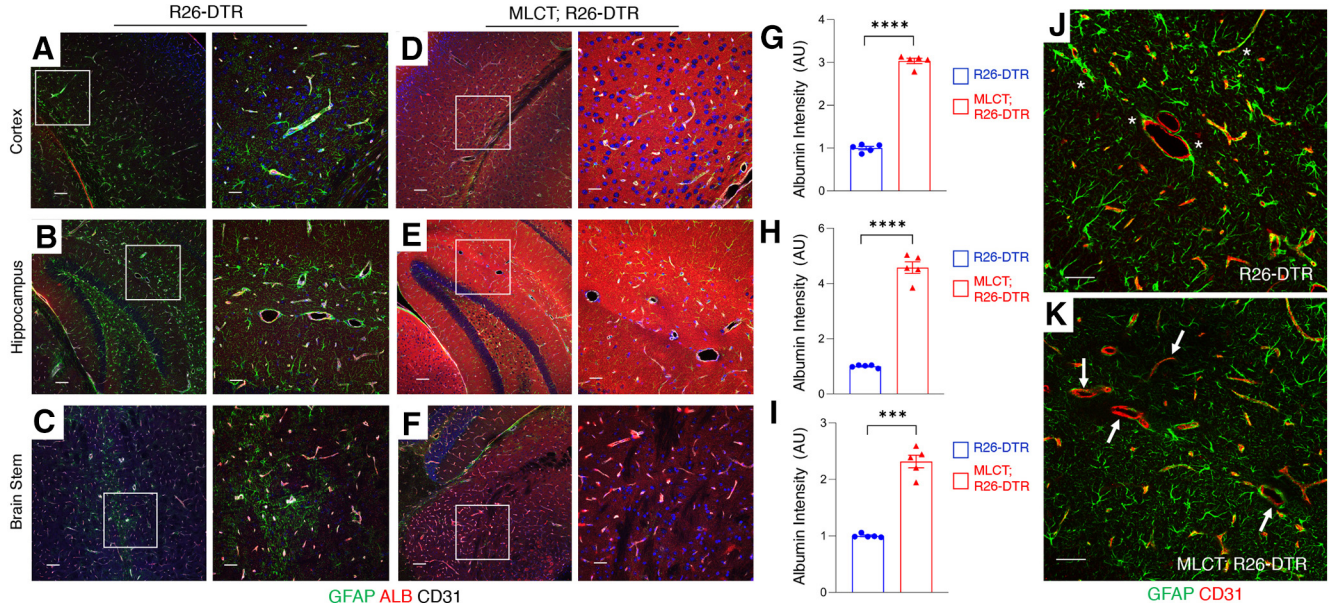

Figure 6. DT-mediated ablation of PAs leads to BBB disruption. ***A–I***, Immunofluorescence analysis of P60 coronal sections from one control (R26-DTR) and a PA-ablated brain (MLCT; R26-DTR) labeled with antibodies directed against GFAP (green), mouse serum albumin (red), and CD31 (white). Shown are representative images from the cerebral cortex (***A***,***D***), hippocampus (***B***,***E***), and brainstem (***C***,***F***). In brain regions from the control mouse, serum albumin is retained in the lumens of cerebral blood vessels (***A–C***), whereas there is robust extravasation of serum albumin into the neural parenchyma of the PA-ablated brains (***D–F***). ***G–I***, Quantitation of mouse serum albumin extravasation in the cortex (***G***), hippocampus (***H***), and brainstem (***I***) of control R26-DTR and MLCT;R26-DTR mutant brains as determined by immunofluorescence intensity. The quantitative data are from images shown in ***A–F***. Differences between groups (***G–I***) were analyzed using Student's *t* test ($n = 3$). Data are mean ± SEM. ***$p < 0.001$. ****$p < 0.0001$. ***J***, ***K***, Analysis of astrocyte interactions with blood vessels in R26-DTR control (***J***) and MLCT;R26-DTR (***K***) mutant brains as determined by double immunofluorescent labeling with anti-GFAP (green) and anti-CD31 (red). Compared with blood vessels in the control brain that are heavily invested by astrocyte end feet (***J***, asterisks), note the reduced coverage of blood vessels by GFAP-expressing astrocytes in the MLCT;R26-DTR mutant brains (***K***, arrows).

data reveal that Mlc1$^+$ astrocyte end feet do not fully ensheath blood vessels in the brain and retina. While there are likely additional perivascular cells that do not express Mlc1, including recently described perivascular fibroblasts (Rajan et al., 2020), our *in vivo* cell ablation data reveal that the Mlc1$^+$ population plays essential roles in stabilization of brain endothelial barrier integrity.

The onset of neurologic deficits in PA-ablated mice, which present several weeks after DT treatment, likely reflects a progressive loss of astrocytes at the neurovascular unit. We speculate that Mlc1$^+$ astrocytes that die following DT treatment may be slowly cycling cells that give rise to more differentiated astrocytes with functions at the BBB. Interestingly, BBB disruption and neurologic deficits were detected at differing levels of severity in the PA-ablated mice, with most animals ($n = 3$) displaying obvious BBB permeability leakage and severe neurodegenerative phenotypes. In contrast, one mutant mouse displayed less severe BBB permeability defects following DT administration. This variability in phenotype is probably related to (1) spatial and temporal differences in tamoxifen-inducible MLCT activation, (2) differences in DTR expression levels following Cre-mediated recombination, and/or (3) heterogeneity in response to DT administration. For example, there is likely brain regional heterogeneity in DTR expression in PAs following tamoxifen delivery to MLCT mice. Nonetheless, it is quite remarkable that ablation of a fairly small subset of PAs can lead to such profound neurovascular deficits and death, which highlights the essential functions of Mlc1$^+$ cells in brain homeostasis.

While this work provides evidence for the role of PA in the maintenance of BBB integrity, future work will focus on elucidating both the developmental fate of PAs and the signaling pathways involved in their functional links to vasculature. Mouse astrocytes are derived from radial glial progenitor cells found within transient germinal centers, including the ganglionic eminences, of the developing brain (Gallo and Deneen, 2014). It will be informative to use the MLCT model to "fate map" select radial glial cell populations that may differentially contribute to astrocytic cell populations in the adult cortex. The MLCT model will also be powerful for selectively targeting gene expression in PAs (and not other astrocyte populations) to elucidate pathways with functional links to the vasculature. Indeed, our prior efforts to engineer the mouse Mlc1 gene to drive GFP expression and fluorescently labeled PAs throughout the adult brain (Toutounchian and McCarty, 2017) have enabled the isolation and transcriptional profiling of these Mlc1-expressing cells (Yosef et al., 2020). Use of the MLCT model to ablate specific genes should yield functional information about pathways in PAs that control the BBB.

Mlc1$^{-/-}$ mice display neurologic pathologies that have some similarities to early stage MLC in humans (Dubey et al., 2015), although Mlc1$^{-/-}$ mice do not fully recapitulate the complex brain pathologies that typify the human disease (Hoegg-Beiler et al., 2014). A recent study has reported normal BBB integrity in Mlc1$^{-/-}$ mice (Gilbert et al., 2021). In the PA-ablated mouse model we describe here, we detect more severe neurologic deficits than those described in Mlc1$^{-/-}$ mice. These data indicate that there are additional PA-enriched gene products in addition to Mlc1 that are required for communication with vascular endothelial cells (and possible pericytes) to collectively control BBB integrity. Ablation of PAs impacts most, if not all, of these pathways, leading to severe BBB breakdown and related neurologic deficits. It will be interesting to quantify levels of PA loss in brain pathologies characterized by BBB leakage, such as stroke. A recent report has shown that GFAP$^+$ reactive astrocytes contribute to vascular repair following ischemic stroke (Williamson et

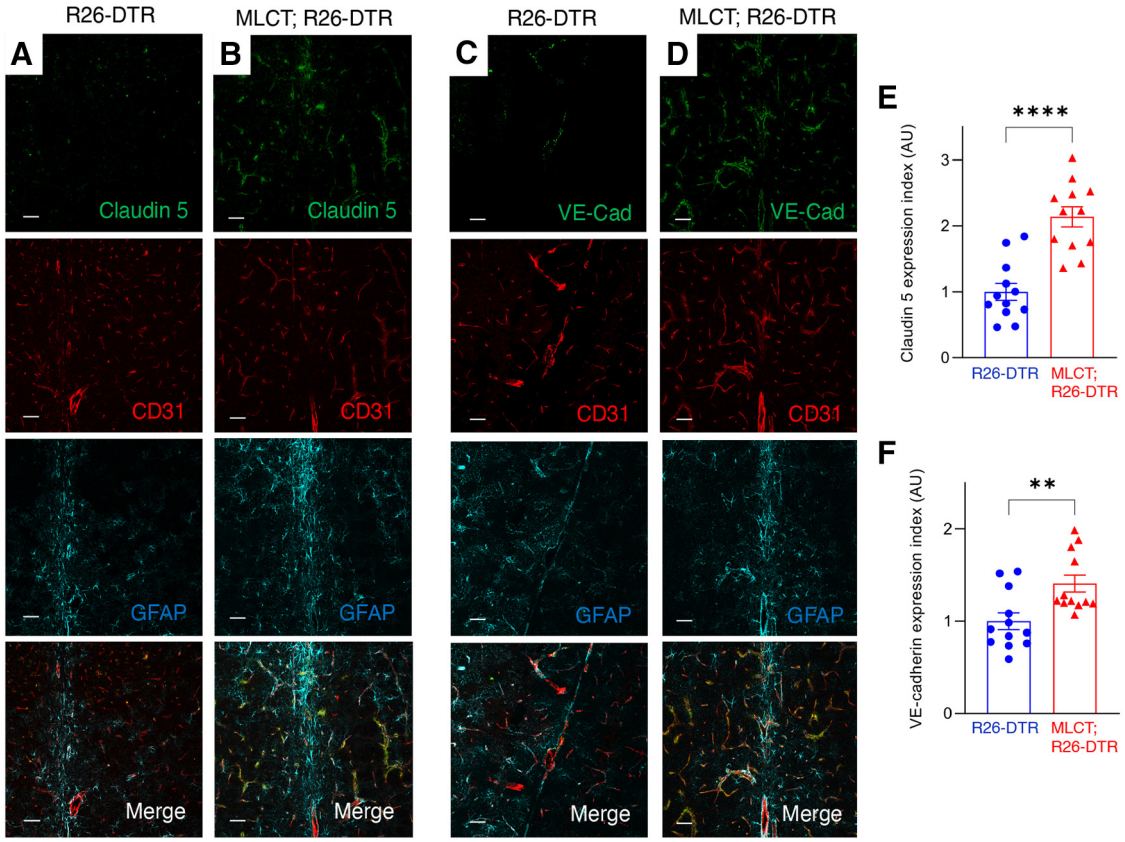

Figure 7. Abnormal localization of endothelial cell junction proteins following ablation of PAs. ***A***, ***B***, Immunofluorescence analysis of P60 coronal sections through the cerebellum from a R26-DTR control (***A***) and MLCT;R26-DTR mutant brain (***B***) labeled with antibodies directed against Cld5 (green), CD31 (red), and GFAP (cyan). Cld5 is focally expressed in endothelial cell tight junctions in the control brain, whereas there is more diffuse expression in the PA-ablated brain vasculature. ***C***, ***D***, Immunofluorescence analysis of P60 coronal sections through the cerebellum from one representative control R26-DTR (***C***) and MLCT;R26-DTR mutant brain (***D***) labeled with antibodies directed against VE-Cadherin (green), CD31 (red), and GFAP (cyan). [dot]VE-Cadherin expression patterns are more diffuse in endothelial cells of the PA-ablated brain. ***E***, ***F***, Quantitation of expression of Claudin 5 (***E***) and VE-Cadherin (***F***) based on immunofluorescence signal. Differences between groups were analyzed using Student's *t* test ($n = 3$). Data are mean ± SEM. $^{**}p < 0.01$. $^{****}p < 0.0001$.

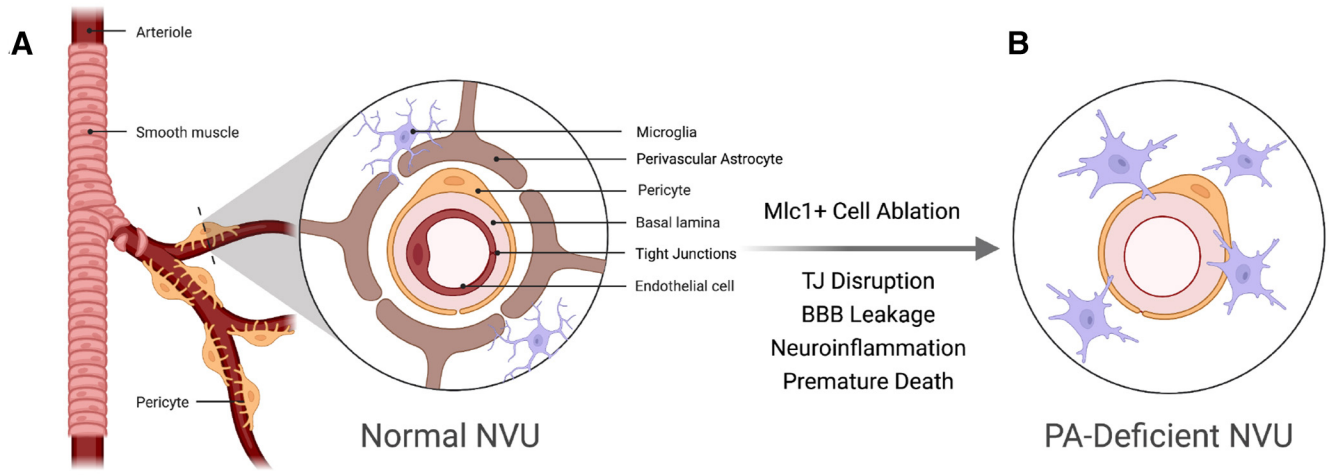

Figure 8. A model for PA-dependent control of BBB integrity in the neurovascular unit. ***A***, In the healthy mammalian brain, PA end feet juxtapose the abluminal surface of cerebral blood vessels and mediate cell-cell contact and communication events between endothelial cells and pericytes within the neurovascular unit (NVU). ***B***, Loss of PAs, or defects in communication with the vascular endothelium, lead to diminished structural stability, defective NVU cytoarchitecture, and failed BBB integrity. PA-derived cues normally control endothelial tight junction protein composition and integrity, as evidenced by the abnormal tight junction composition and BBB disruption following PA ablation. This figure was created with https://biorender.com/.

al., 2021). Determining whether Mlc1-expressing PAs are a part of this reactive component and quantifying their relative contributions to blood vessel repair will be informative. Last, while efforts to study neurologic diseases linked to BBB breakdown have mainly focused on defective signaling events in vascular endothelial cells and/or neurons (Cunha et al., 2017), defects in PAs may also be important. Therefore, we propose that PA dysfunction may be an underlying cause for the

onset and progression of heritable vascular-related neurologic pathologies.

References

Alonso-Gardon M, Elorza-Vidal X, Castellanos A, La Sala G, Armand-Ugon M, Gilbert A, Di Pietro C, Pla-Casillanis A, Ciruela F, Gasull X, Nunes V, Martinez A, Schulte U, Cohen-Salmon M, Marazziti D, Estévez R (2021) Identification of the GlialCAM interactome: the G protein-coupled receptors GPRC5B and GPR37L1 modulate Megalencephalic leukoencephalopathy proteins. Hum Mol Genet 30:1649–1665.

Boor PK, de Groot K, Waisfisz Q, Kamphorst W, Oudejans CB, Powers JM, Pronk JC, Scheper GC, van der Knaap MS (2005) MLC1: a novel protein in distal astroglial processes. J Neuropathol Exp Neurol 64:412–419.

Brignone MS, Lanciotti A, Serafini B, Mallozzi C, Sbriccoli M, Veroni C, Molinari P, Elorza-Vidal X, Petrucci TC, Estévez R, Ambrosini E (2019) Megalencephalic leukoencephalopathy with subcortical cysts protein-1 (MLC1) counteracts astrocyte activation in response to inflammatory signals. Mol Neurobiol 56:8237–8254.

Buch T, Heppner FL, Tertilt C, Heinen TJ, Kremer M, Wunderlich FT, Jung S, Waisman A (2005) A Cre-inducible diphtheria toxin receptor mediates cell lineage ablation after toxin administration. Nat Methods 2:419–426.

Cleaver O (2021) Mouse models of vascular development and disease. Curr Opin Hematol 28:179–188.

Cohen-Salmon M, Slaoui L, Mazare N, Gilbert A, Oudart M, Alvear-Perez R, Elorza-Vidal X, Chever O, Boulay AC (2021) Astrocytes in the regulation of cerebrovascular functions. Glia 69:817–841.

Cunha SI, Magnusson PU, Dejana E, Lampugnani MG (2017) Deregulated TGF-beta/BMP signaling in vascular malformations. Circ Res 121:981–999.

Dubey M, Bugiani M, Ridder MC, Postma NL, Brouwers E, Polder E, Jacobs JG, Baayen JC, Klooster J, Kamermans M, Aardse R, de Kock CP, Dekker MP, van Weering JR, Heine VM, Abbink TE, Scheper GC, Boor I, Lodder JC, Mansvelder HD, et al. (2015) Mice with megalencephalic leukoencephalopathy with cysts: a developmental angle. Ann Neurol 77:114–131.

Dubey M, Brouwers E, Hamilton EM, Stiedl O, Bugiani M, Koch H, Kole MH, Boschert U, Wykes RC, Mansvelder HD, van der Knaap MS, Min R (2018) Seizures and disturbed brain potassium dynamics in the leukodystrophy megalencephalic leukoencephalopathy with subcortical cysts. Ann Neurol 83:636–649.

Estévez R, Elorza-Vidal X, Gaitán-Peñas H, Pérez-Rius C, Armand-Ugón M, Alonso-Gardón M, Xicoy-Espaulella E, Sirisi S, Arnedo T, Capdevila-Nortes X, López-Hernández T, Montolio M, Duarri A, Teijido O, Barrallo-Gimeno A, Palacín M, Nunes V (2018) Megalencephalic leukoencephalopathy with subcortical cysts: a personal biochemical retrospective. Eur J Med Genet 61:50–60.

Foo LC, Allen NJ, Bushong EA, Ventura PB, Chung WS, Zhou L, Cahoy JD, Daneman R, Zong H, Ellisman MH, Barres BA (2011) Development of a method for the purification and culture of rodent astrocytes. Neuron 71:799–811.

Gaitán-Peñas H, Apaja PM, Arnedo T, Castellanos A, Elorza-Vidal X, Soto D, Gasull X, Lukacs GL, Estévez R (2017) Leukoencephalopathy-causing CLCN2 mutations are associated with impaired Cl(-) channel function and trafficking. J Physiol 595:6993–7008.

Gallo V, Deneen B (2014) Glial development: the crossroads of regeneration and repair in the CNS. Neuron 83:283–308.

Gilbert A, Elorza-Vidal X, Rancillac A, Chagnot A, Yetim M, Hingot V, Deffieux T, Boulay AC, Alvear-Perez R, Cisternino S, Martin S, Taïb S, Gelot A, Mignon V, Favier M, Brunet I, Declèves X, Tanter M, Estévez R, Vivien D, et al. (2021) Megalencephalic leukoencephalopathy with subcortical cysts is a developmental disorder of the gliovascular unit. Elife 10:e71379.

Guo D, Zou J, Rensing N, Wong M (2017) In vivo two-photon imaging of astrocytes in GFAP-GFP transgenic mice. PLoS One 12:e0170005.

Heinemann U, Kaufer D, Friedman A (2012) Blood–brain barrier dysfunction, TGFbeta signaling, and astrocyte dysfunction in epilepsy. Glia 60:1251–1257.

Heithoff BP, George KK, Phares AN, Zuidhoek IA, Munoz-Ballester C, Robel S (2021) Astrocytes are necessary for blood–brain barrier maintenance in the adult mouse brain. Glia 69:436–472.

Helms HC, Abbott NJ, Burek M, Cecchelli R, Couraud PO, Deli MA, Forster C, Galla HJ, Romero IA, Shusta EV, Stebbins MJ, Vandenhaute E, Weksler B, Brodin B (2016) In vitro models of the blood–brain barrier: an overview of commonly used brain endothelial cell culture models and guidelines for their use. J Cereb Blood Flow Metab 36:862–890.

Hirota S, Clements TP, Tang LK, Morales JE, Lee HS, Oh SP, Rivera GM, Wagner DS, McCarty JH (2015) Neuropilin 1 balances beta8 integrin-activated TGFbeta signaling to control sprouting angiogenesis in the brain. Development 142:4363–4373.

Hoegg-Beiler MB, Sirisi S, Orozco IJ, Ferrer I, Hohensee S, Auberson M, Gödde K, Vilches C, de Heredia ML, Nunes V, Estévez R, Jentsch TJ (2014) Disrupting MLC1 and GlialCAM and ClC-2 interactions in leukodystrophy entails glial chloride channel dysfunction. Nat Commun 5:3475.

Holash JA, Noden DM, Stewart PA (1993) Re-evaluating the role of astrocytes in blood–brain barrier induction. Dev Dyn 197:14–25.

Janzer RC, Raff MC (1987) Astrocytes induce blood–brain barrier properties in endothelial cells. Nature 325:253–257.

Khakh BS, Deneen B (2019) The emerging nature of astrocyte diversity. Annu Rev Neurosci 42:187–207.

Korogod N, Petersen CC, Knott GW (2015) Ultrastructural analysis of adult mouse neocortex comparing aldehyde perfusion with cryo fixation. Elife 4:e05793.

Lanciotti A, Brignone MS, Belfiore M, Columba-Cabezas S, Mallozzi C, Vincentini O, Molinari P, Petrucci TC, Visentin S, Ambrosini E (2020) Megalencephalic leukoencephalopathy with subcortical cysts disease-linked MLC1 protein favors gap-junction intercellular communication by regulating connexin 43 trafficking in astrocytes. Cells 9:1425.

Lattier JM, De A, Chen Z, Morales JE, Lang FF, Huse JT, McCarty JH (2020) Megalencephalic leukoencephalopathy with subcortical cysts 1 (MLC1) promotes glioblastoma cell invasion in the brain microenvironment. Oncogene 39:7253–7264.

Lee HS, Cheerathodi M, Chaki SP, Reyes SB, Zheng Y, Lu Z, Paidassi H, DerMardirossian C, Lacy-Hulbert A, Rivera GM, McCarty JH (2015) Protein tyrosine phosphatase-PEST and beta8 integrin regulate spatiotemporal patterns of RhoGDI1 activation in migrating cells. Mol Cell Biol 35:1401–1413.

MacVicar BA, Newman EA (2015) Astrocyte regulation of blood flow in the brain. Cold Spring Harb Perspect Biol 7:a020388.

McCarty JH (2020) αvβ8 integrin adhesion and signaling pathways in development, physiology and disease. J Cell Sci 133:jcs239434.

O'Brown NM, Pfau SJ, Gu C (2018) Bridging barriers: a comparative look at the blood–brain barrier across organisms. Genes Dev 32:466–478.

Rahimi N (2017) Defenders and challengers of endothelial barrier function. Front Immunol 8:1847.

Rajan AM, Ma RC, Kocha KM, Zhang DJ, Huang P (2020) Dual function of perivascular fibroblasts in vascular stabilization in zebrafish. PLoS Genet 16:e1008800.

Rasmussen MK, Mestre H, Nedergaard M (2018) The glymphatic pathway in neurological disorders. Lancet Neurol 17:1016–1024.

Regan MR, Huang YH, Kim YS, Dykes-Hoberg MI, Jin L, Watkins AM, Bergles DE, Rothstein JD (2007) Variations in promoter activity reveal a differential expression and physiology of glutamate transporters by glia in the developing and mature CNS. J Neurosci 27:6607–6619.

Rueden CT, Schindelin J, Hiner MC, DeZonia BE, Walter AE, Arena ET, Eliceiri KW (2017) ImageJ2: ImageJ for the next generation of scientific image data. BMC Bioinformatics 18:529.

Saunders NR, Dziegielewska KM, Mollgard K, Habgood MD (2018) Physiology and molecular biology of barrier mechanisms in the fetal and neonatal brain. J Physiol 596:5723–5756.

Schindelin J, Arganda-Carreras I, Frise E, Kaynig V, Longair M, Pietzsch T, Preibisch S, Rueden C, Saalfeld S, Schmid B, Tinevez JY, White DJ, Hartenstein V, Eliceiri K, Tomancak P, Cardona A (2012) Fiji: an open-source platform for biological-image analysis. Nat Methods 9:676–682.

Schneider CA, Rasband WS, Eliceiri KW (2012) NIH Image to ImageJ: 25 years of image analysis. Nat Methods 9:671–675.

Senatorov VV Jr, Friedman AR, Milikovsky DZ, Ofer J, Saar-Ashkenazy R, Charbash A, Jahan N, Chin G, Mihaly E, Lin JM, Ramsay HJ, Moghbel A, Preininger MK, Eddings CR, Harrison HV, Patel R, Shen Y, Ghanim H, Sheng H, Veksler R, et al. (2019) Blood–brain barrier dysfunction in aging induces hyperactivation of TGFbeta signaling and chronic yet reversible neural dysfunction. Sci Transl Med 11:eaaw8283.

Srinivas S, Watanabe T, Lin CS, William CM, Tanabe Y, Jessell TM, Costantini F (2001) Cre reporter strains produced by targeted insertion of EYFP and ECFP into the ROSA26 locus. BMC Dev Biol 1:4.

Toutounchian JJ, McCarty JH (2017) Selective expression of eGFP in mouse perivascular astrocytes by modification of the Mlc1 gene using T2A-based ribosome skipping. Genesis 55:e23071.

van der Knaap MS, Boor I, Estévez R (2012) Megalencephalic leukoencephalopathy with subcortical cysts: chronic white matter oedema due to a defect in brain ion and water homoeostasis. Lancet Neurol 11:973–985.

Vanlandewijck M, He L, Mae MA, Andrae J, Ando K, Del Gaudio F, Nahar K, Lebouvier T, Lavina B, Gouveia L, Sun Y, Raschperger E, Rasanen M, Zarb Y, Mochizuki N, Keller A, Lendahl U, Betsholtz C (2018) A molecular atlas of cell types and zonation in the brain vasculature. Nature 554:475–480.

Wang MX, Ray L, Tanaka KF, Iliff JJ, Heys J (2021) Varying perivascular astroglial endfoot dimensions along the vascular tree maintain perivascular-interstitial flux through the cortical mantle. Glia 69:715–728.

Williamson MR, Fuertes CJ, Dunn AK, Drew MR, Jones TA (2021) Reactive astrocytes facilitate vascular repair and remodeling after stroke. Cell Rep 35:109048.

Winchenbach J, Duking T, Berghoff SA, Stumpf SK, Hulsmann S, Nave KA, Saher G (2016) Inducible targeting of CNS astrocytes in Aldh1l1-CreERT2 BAC transgenic mice. F1000Res 5:2934.

Yosef N, Xi Y, McCarty JH (2020) Isolation and transcriptional characterization of mouse perivascular astrocytes. PLoS One 15:e0240035.

Zajec M, Kros JM, Dekker-Nijholt DA, Dekker LJ, Stingl C, van der Weiden M, van den Bosch TP, Mustafa DA, Luider TM (2021) Identification of blood–brain barrier-associated proteins in the human brain. J Proteome Res 20:531–537.

Zarei-Kheirabadi M, Vaccaro AR, Rahimi-Movaghar V, Kiani S, Baharvand H (2020) An overview of extrinsic and intrinsic mechanisms involved in astrocyte development in the central nervous system. Stem Cells Dev 29:266–280.

Zhang Y, Chen K, Sloan SA, Bennett ML, Scholze AR, O'Keeffe S, Phatnani HP, Guarnieri P, Caneda C, Ruderisch N, Deng S, Liddelow SA, Zhang C, Daneman R, Maniatis T, Barres BA, Wu JQ (2014) An RNA-sequencing transcriptome and splicing database of glia, neurons, and vascular cells of the cerebral cortex. J Neurosci 34:11929–11947.